

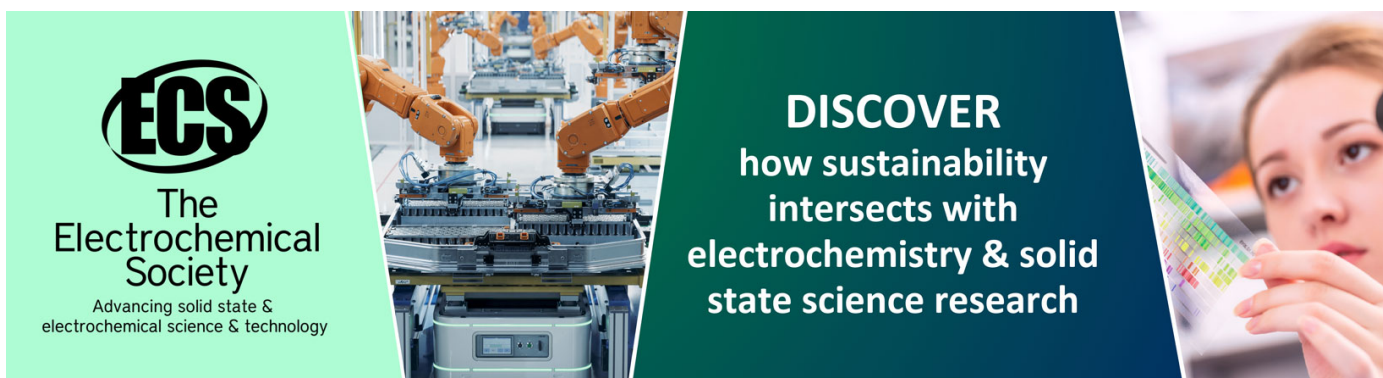
Dynamics of magnetic nanoparticle suspensions

To cite this article: Vanchna Singh *et al* 2009 *J. Phys. D: Appl. Phys.* **42** 245006

View the [article online](#) for updates and enhancements.

You may also like

- [Scalar field cosmology modified by the generalized uncertainty principle](#)
Andronikos Paliathanasis, Supriya Pan and Souvik Pramanik
- [On the uniqueness of supersymmetric AdS\(5\) black holes with toric symmetry](#)
James Lucietti, Praxitelis Ntokos and Sergei G Ovchinnikov
- [Magnetic nanoparticle thermometry independent of Brownian relaxation](#)
Jing Zhong, Meinhard Schilling and Frank Ludwig



ECS
The
Electrochemical
Society
Advancing solid state &
electrochemical science & technology

DISCOVER
how sustainability
intersects with
electrochemistry & solid
state science research

Dynamics of magnetic nanoparticle suspensions

Vanchna Singh¹, Varsha Banerjee¹ and Manish Sharma²

¹ Department of Physics, Indian Institute of Technology, Hauz Khas, New Delhi 110016, India

² Centre for Applied Research in Electronics, Indian Institute of Technology, Hauz Khas, New Delhi 110016, India

Received 6 July 2009, in final form 30 October 2009

Published 26 November 2009

Online at stacks.iop.org/JPhysD/42/245006

Abstract

We study the dynamical response of suspensions of single-domain magnetic nanoparticles. The effect of sample parameters on Néel and Brownian relaxation times which characterize the response is studied. Their effect on the ac susceptibility is also investigated. As the relaxation times are strongly size dependent we study the effect of polydispersity on the response functions next. A procedure to extract particle-size distribution in polydisperse samples from Cole–Cole plots is provided. Further, the presence of attractive and repulsive interactions amongst MNP yields a distribution of clusters of varying sizes. We propose a model incorporating the phenomena of aggregation and fragmentation to understand the formation of clusters and their distributions. Finally, we compare our numerical results with the experimental data. These comparisons are satisfactory.

1. Introduction

Single-domain magnetic nanoparticles (MNPs) and their colloidal suspensions have attracted a lot of attention in recent years [1–4]. The growing interest is due to a variety of technological applications associated with them. These range from mechanical and thermal applications involving their usage as sealants, lubricants and coolants to challenging applications in medicine for the purpose of magnetic resonance imaging, targeted drug delivery and biomarkers and biosensors to name a few. The main reason behind their wide applicability is the ease with which they can be detected and manipulated by the application of an external magnetic field. Their response times are strongly size dependent, thus introducing the possibility of synthesizing particles to yield application tailored response times.

Most practical applications require surfactant coatings to prevent agglomeration and sedimentation of MNPs. Many biological and medical applications require nanoparticles with biologically relevant coatings in order to use them as probes and carriers [4–6]. The Néel and Brownian relaxation times which characterize the dynamics of the suspension depend not only upon the constituting material but also upon the magnetic volume and the enhanced volume due to surfactant coating. In this paper, we systematically analyse the effect of the above parameters on the relaxation times. We also study

their effect on the ac susceptibility $\chi(\omega)$, which is the most commonly studied response function in the laboratory. As the Néel and Brownian relaxation times have a strong dependence on particle size, we find that polydispersity (inherent in experimental samples) results in significant changes in the response function. We have also worked out a procedure to obtain particle-size distributions from the susceptibility data via Cole–Cole plots when they are unavailable.

The above approach assumes the *single-particle model* [7] applicable to dilute suspensions in which magnetic interactions amongst particles may be ignored. When present in sufficient concentration, clustering and chaining of MNP are rather common as observed by electron microscopy or dynamic light scattering studies [8–10]. This behaviour is undesirable in many applications using magnetic fluids as sealants, coolants, lubricants, printing inks, etc. where invariance of the magnetic and fluid properties are paramount [1]. On the other hand, magnetic domain detection, optical shutters, tagging of surfaces and other entities benefit from clustering of MNP [1, 11]. It is hence useful to understand clustering and its dependence on sample parameters to introduce the possibility of application tailored suspensions. In this spirit, we introduce a model incorporating the competing mechanisms of aggregation and fragmentation. We obtain steady-state cluster-size distributions and mean-cluster sizes for different ratios characterizing the relative strengths of the aggregation and

fragmentation processes. Both these functions exhibit scaling. We have then compared our results with sets of experimental data to lend credence to the aggregation–fragmentation model.

The paper is organized as follows. Section 2 deals with relaxation mechanisms and response functions of dilute MNP suspensions. In section 2.1, we introduce the Néel and Brownian relaxation times and identify regimes where either or both relaxation times contribute. Polydispersity and its characterization is introduced in section 2.2. The calculation of the ac susceptibility $\chi(\omega)$ for monodisperse and polydisperse samples in the different regimes described above is presented in section 2.3. In section 2.4, we provide a procedure to obtain particle-size distributions (for polydisperse samples) using Cole–Cole plots. Section 3 deals with aspects of clustering occurring in samples which are no longer governed by the single-particle approximation. Interactions responsible for clustering are introduced in section 3.1. We introduce the aggregation–fragmentation model in section 3.2. The numerical results are presented in section 3.3. Their comparisons with corresponding measurements in a variety of experimental systems are presented in section 3.4. Finally, we conclude this paper with a summary of results in section 4.

2. Relaxation mechanisms and response functions of dilute MNP suspensions

We now study the relaxation properties and the response functions in dilute MNP suspensions where inter-particle interactions can be ignored. In this regime the particles essentially behave as independent, single-domain, super paramagnetic entities.

2.1. Néel and Brownian relaxation times

If we assume that the anisotropy responsible for single-domain MNP is uniaxial (in the z -direction say), the magnetic energy is given by [12]

$$E = VK \sin^2 \theta, \quad (1)$$

where $V = 4\pi r_c^3/3$ is the magnetic volume of a particle with radius r_c usually referred to as the core radius, K is the effective magnetic anisotropy constant and θ is the angle between the z -axis and \hat{n} . Minimum energy occurs at $\theta = 0$ and π defining two equilibrium orientations corresponding to magnetizations $+VM_o$ and $-VM_o$. If thermal fluctuations are strong enough, magnetic moment reversal takes place within the particle by overcoming the energy barrier (of height VK). As a result the time-averaged magnetization is zero and the particle is paramagnetic. The reversal or switching time is called the Néel relaxation time and is given by

$$\tau_N = \tau_o e^{VK/k_B T}, \quad (2)$$

where τ_o is related to the inverse of the attempt frequency of magnetic reversal.

There is another mechanism by which the magnetic moment of a super paramagnetic particle suspended in a fluid can relax. This mechanism of relaxation can be due to the physical rotation of the particle within the fluid. It is referred

to as Brownian rotational motion as it occurs due to the thermal fluctuations in the suspended medium. The Brownian relaxation time is given by [3, 13]

$$\tau_B = \frac{4\pi\eta r_h^3}{k_B T}, \quad (3)$$

where η is the dynamic viscosity of carrier liquid and r_h is the hydrodynamic radius defined as the sum of the core radius r_c of the MNP and the surfactant coating δ over it.

As can be seen from equations (2) and (3), both Néel and Brownian relaxation times are highly sensitive to the particle size. While τ_N increases exponentially, τ_B grows linearly with the particle dimension. It is customary to define an effective relaxation time as follows [7, 14]:

$$\frac{1}{\tau_e} = \frac{1}{\tau_N} + \frac{1}{\tau_B}$$

or

$$\tau_e = \frac{\tau_N + \tau_B}{\tau_N \tau_B}. \quad (4)$$

Thus, it is possible to tailor time scales by an appropriate choice of parameters, particularly K , r_c and r_h . With this in mind, we have systematically studied the effect of r_c and r_h on τ_N and τ_B and consequently τ_e for maghemite (Fe_3O_4) particles used most commonly in making magnetic fluids.

In table 1, we summarize our evaluations of τ_N , τ_B and τ_e for particles with varying magnetic core radius r_c and the thickness of the surfactant coating δ . In most experiments, the latter is usually in the range 2–6 nm. As observed in table 1, τ_B is practically unaffected by δ . For small particles, $\tau_N \ll \tau_B$ which results in $\tau_e \approx \tau_N$. The relaxation then takes place by rotation of the magnetic moment inside the particle. For large particles, on the other hand, $\tau_B \ll \tau_N$. Consequently, $\tau_e \approx \tau_B$ and the relaxation is due to a physical rotation of the particle in the suspension. Thus, the choice of the relaxation mode is primarily governed by the particle size. For critical particle sizes, often called the cross-over radius r^* (~ 8 nm in table 1), it is found that both mechanisms contribute to the relaxation of the suspended particle.

We have studied the effect of temperature T , the surfactant coating δ and the anisotropy constant K on the cross-over radius r^* . Most applications require an operating temperature in the range 270–320 K. We find that r^* does not change perceptibly in this range. Further, as seen from table 1 the variation of δ does not significantly alter r^* . The anisotropy constant K , on the other hand, leads to a substantial change in the corresponding value of the cross-over radius. For instance, our evaluations show that spherical MNP of Co having an anisotropy constant $K = 4 \times 10^6 \text{ J m}^{-3}$ has $r^* \sim 2.5$ nm while spherical MNP of Fe having an anisotropy constant $K = 4 \times 10^5 \text{ J m}^{-3}$ has $r^* \sim 5$ nm. Thus, amongst the three parameters of relevance, the anisotropy constant K affects the cross-over radius r^* the most.

2.2. Polydispersity

Monodisperse samples are an idealization. All experimental samples have a distribution of particle sizes and are referred

Table 1. Variation of the Néel (τ_N), Brownian (τ_B) and effective (τ_e) relaxation times as a function of the core radius r_c of the MNPs. τ_B has also been evaluated for three values of the surfactant coating δ . The corresponding τ_e for these values is also evaluated.

r_c (nm)	τ_N (s)	τ_B			τ_e (s)		
		$\delta_1 = 2$ nm	$\delta_2 = 4$ nm	$\delta_3 = 6$ nm	τ_{e1}	τ_{e2}	τ_{e3}
4	10^{-9}	10^{-7}	10^{-6}	10^{-6}	10^{-9}	10^{-9}	10^{-9}
6	10^{-8}	10^{-6}	10^{-6}	10^{-6}	10^{-8}	10^{-8}	10^{-8}
8	10^{-5}	10^{-6}	10^{-6}	10^{-6}	10^{-6}	10^{-6}	10^{-6}
10	10^{-1}	10^{-6}	10^{-6}	10^{-5}	10^{-6}	10^{-6}	10^{-5}
15	10^{20}	10^{-5}	10^{-5}	10^{-5}	10^{-5}	10^{-5}	10^{-5}
20	10^{61}	10^{-5}	10^{-5}	10^{-5}	10^{-5}	10^{-5}	10^{-5}

to as polydispersity. Transmission electron microscopy (TEM) studies of several samples have revealed a log-normal distribution for the variation of particle sizes [1, 14, 15]. Thus, the probability density $P(r_c) dr_c$ of having particles within radius r_c and $r_c + dr_c$ can be written as

$$P(r_c) dr_c = \frac{1}{\sqrt{2\pi \ln \sigma}} \exp \left[-\ln^2(r_c/\bar{r}_c)/(2 \ln^2 \sigma) \right] dr_c, \quad (5)$$

where \bar{r}_c and σ are the mean and variance of the distribution. Due to the strong dependence of both Néel and Brownian relaxation times on particle size, it is evident that a distribution of relaxation times will be obtained if the suspended particles have a distribution of sizes. The presence of polydispersity leads to a significant change in the behaviour of the response function of the sample as we shall see in the following subsection.

2.3. Ac susceptibility measurements

The complex susceptibility $\chi(\omega)$ of a suspension of monodisperse MNP in the linear response regime has the Debye form given by [12]

$$\chi(\omega) = \frac{\chi_0}{(1 - i\omega\tau_e)}, \quad (6)$$

where $\chi_0 = \chi(\omega = 0) = NV^2M_0^2/k_B T$ is the static susceptibility of the sample comprising N monodisperse particles of volume V with a saturation magnetization M_0 . The effective relaxation time τ_e is defined by equation (4).

The susceptibility response gets substantially altered in the presence of polydispersity. For polydisperse samples $\chi(\omega)$ needs to be averaged over the particle-size distribution $P(r_c)$. Thus,

$$\chi'(\omega) = \chi_0 \int dr_c P(r_c) \frac{1}{1 + \omega^2 \tau_e^2(r_c)} \quad (7)$$

and

$$\chi''(\omega) = \chi_0 \int dr_c P(r_c) \frac{\omega \tau_e(r_c)}{1 + \omega^2 \tau_e^2(r_c)}. \quad (8)$$

In the case of monodisperse samples, $\chi''(\omega)$ versus ω exhibits a symmetric Debye peak around $\omega = \tau_e^{-1}$.

In figure 1, we plot $\chi''(\omega)$ for monodisperse samples (open circles) corresponding to three different values of $r_c = 4, 8$ and 12 nm. The chosen values correspond to (a) $r_c < r^*$, (b) $r_c \approx r^*$ and (c) $r_c > r^*$, respectively, for maghemite particles used to generate data of table 1. All cases exhibit the characteristic Debye form. To understand the effect

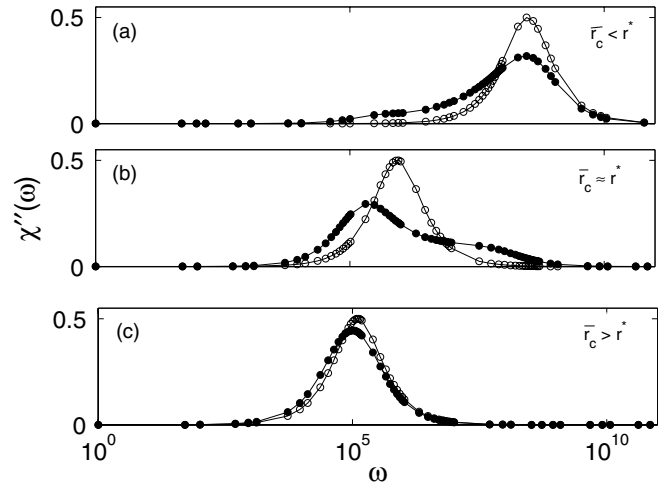


Figure 1. Variation of $\chi''(\omega)$ versus ω for monodisperse (open circles) and polydisperse (filled circles) maghemite samples when (a) $\bar{r}_c < r^*$ and Néel relaxation dominates, (b) $\bar{r}_c \approx r^*$ and both Néel and Brownian relaxations contribute and (c) $\bar{r}_c > r^*$ and Brownian relaxation dominates. The values of \bar{r}_c in (a), (b) and (c) have been chosen as 4 nm, 8 nm and 12 nm, respectively. The surfactant coating δ and the temperature T were taken to be 2 nm and 300 K, respectively, in these evaluations.

of polydispersity, we also plot equation (8) (filled circles) in the same figure. The distribution $P(r_c)$ versus r_c used for the evaluations were obtained from a TEM analysis of maghemite samples used in [14]. These distributions had a log-normal form with a variance $\sigma \approx 0.35$. The mean value \bar{r}_c is the particle size of the corresponding monodisperse evaluation.

As seen in figure 1, a broadening of the response function is observed in all cases after the inclusion of polydispersity. The response no longer has the symmetric Debye form. In figure 1(a), the peak frequency provides information about the mean core radius \bar{r}_c . The width of the log-normal distribution often gives rise to a small Brownian peak although $\bar{r}_c < r^*$ and the particles predominantly exhibit Néel relaxation. A pronounced two-peak response is obtained in figure 1(b) since $\bar{r}_c \approx r^*$. Both Néel and Brownian relaxations contribute in this regime, the latter being the dominant mode. The larger (Brownian) peak is an indication that a larger number of particles are primarily undergoing Brownian relaxation. The frequencies of the peak values yield information about the average values of core and the hydrodynamic radii \bar{r}_c and \bar{r}_h of the particles. Finally, when $\bar{r}_c > r^*$, the Brownian

relaxation dominates and the frequency corresponding to the peak provides information regarding the hydrodynamic radius \bar{r}_h of the particle. Comparing figures 1(a) and (c), it is clear that polydispersity affects Néel relaxation more significantly than Brownian relaxation as expected (cf equations (2) and (3)).

2.4. Particle size distributions from Cole–Cole plots

The information on distribution of relaxation times can be obtained from susceptibility measurements by empirical models. The most frequently used models for this purpose are the Cole–Cole and the Cole–Davidson models. The Cole–Cole model is suitable for systems exhibiting a symmetrical form of $\chi''(\omega)$ about a vertical axis passing through its peak value [16, 17]. The Cole–Davidson model, on the other hand, is employed for asymmetrical forms of $\chi''(\omega)$.

As observed in figure 1, the response functions of typical MNP suspensions are indeed asymmetrical. Therefore, these can be conveniently represented by the Cole–Davidson expression for the ac susceptibility [18]:

$$\chi(\omega) = \frac{\chi_c}{(1 + i\omega\tau_c)^\beta}, \quad (9)$$

where τ_c is the central relaxation time about which all the other relaxation times are distributed and β is a fitting parameter with limits $0 \leq \beta \leq 1$. When $\beta = 1$, the above equation reduces to the Debye form of equation (6) characterized by a single relaxation time. Separating the real and imaginary parts of equation (9) results in

$$\chi'(\omega) = \chi_o \cos \phi^\beta \cos \beta\phi \quad (10)$$

and

$$\chi''(\omega) = \chi_o \cos \phi^\beta \sin \beta\phi, \quad (11)$$

where $\phi = \arctan \omega\tau_c$.

Cole and Cole proposed a method of graphically representing the effects of multiple relaxation times [16, 17]. The method consists of plotting $\chi''(\omega)$ for a certain frequency against $\chi'(\omega)$ at the same frequency. When $\beta = 1$, the Cole–Cole plot is semicircular. The plot is symmetrical about the vertical line passing through the point $\chi'(\omega) = \chi_o/2$ when $\chi''(\omega)$ is maximum at a frequency $\omega = \tau_c^{-1}$. Other values of β yield a ‘skewed arc’ in the Cole–Cole plots which characterizes the presence of multiple relaxation times. The parameter β can be determined from the Cole–Cole plot by a graphical construction. It may also be determined by the best fits of equations (10) and (11) to the experimental data.

In figure 2 we show the Cole–Cole plots for the same polydisperse samples that were used to obtain data of figure 1. Cases (a), (b) and (c) correspond to $\bar{r}_c < r^*$, $\bar{r}_c \approx r^*$ and $\bar{r}_c > r^*$, respectively. The skewed arcs observed in all the cases are a consequence of multiple relaxation times introduced due to polydispersity in the samples. Further, the asymmetry in the particle-size distributions is reflected in the asymmetry of the arcs. The Cole–Cole plots are distinct in each of the regimes. In particular, the cross-over regime is characterized by a two-humped form signifying a

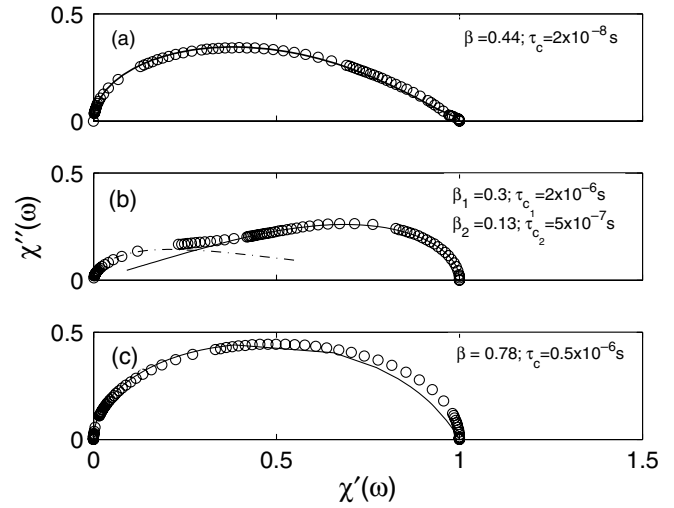


Figure 2. Cole–Cole plots (open circles) for data of figure 1 when (a) $\bar{r}_c < r^*$ and Néel relaxation dominates, (b) $\bar{r}_c \approx r^*$ and both Néel and Brownian relaxations contribute and (c) $\bar{r}_c > r^*$ and Brownian relaxation dominates. The plots exhibit a two-humped structure when both relaxation times contribute (case b). The β and the τ_c values obtained from the Cole–Davidson equations are also indicated in the figures.

contribution of both Néel and Brownian relaxations to the response function. Thus, significant information regarding the experimental sample can be inferred from the Cole–Cole plots.

We now provide a simple procedure for evaluating the particle-size distribution $P(r_c)$ versus r_c in the experimental sample when the response function exhibits multiple relaxation times. Assuming a log-normal form, $P(r_c)$ versus r_c is characterized by its mean \bar{r}_c and variance σ signifying the spread in the particle-size distributions. While the evaluation of \bar{r}_c is straightforward, the variance σ needs to be estimated. Recalling that multiple relaxation times are a consequence of polydispersity, it is imperative to connect β with σ . In order to find this relationship, we have gone through the following sequence of steps. Firstly, $\chi'(\omega)$ and $\chi''(\omega)$ were evaluated using equations (7) and (8) for a chosen value of \bar{r}_c and σ . The corresponding values of τ_c and β were then obtained by fitting the above susceptibility data with equations (10) and (11) of the Cole–Davidson model. This procedure was then repeated for a number of σ values in the range 0.1–0.5, keeping \bar{r}_c constant. Larger values of σ were not considered as they resulted in extremely broad log-normal distributions which are not of relevance in experiments. The above evaluation was then performed for three different values of K . The results obtained are plotted in figure 3 on a semi-logarithmic scale. The solid lines follow the equation

$$\sigma = A(K)e^{-B\beta}. \quad (12)$$

The parameters $A(K)$ and B in each case are obtained from the best fits of the above equation to the evaluated data. We find that $B = 2.45 \pm 0.05$ and is independent of K . We also find that equation (12) and the parameter B are unaffected by \bar{r}_c , which was varied from 4 to 12 nm.

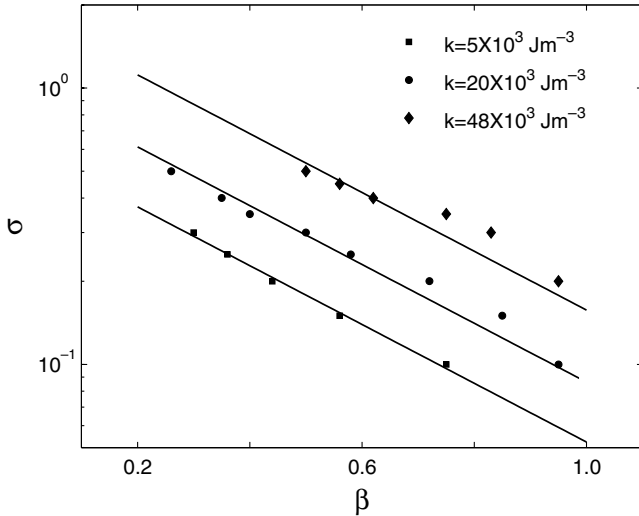


Figure 3. Variation of σ as a function of β for three different anisotropy constants on a semi-logarithmic scale.

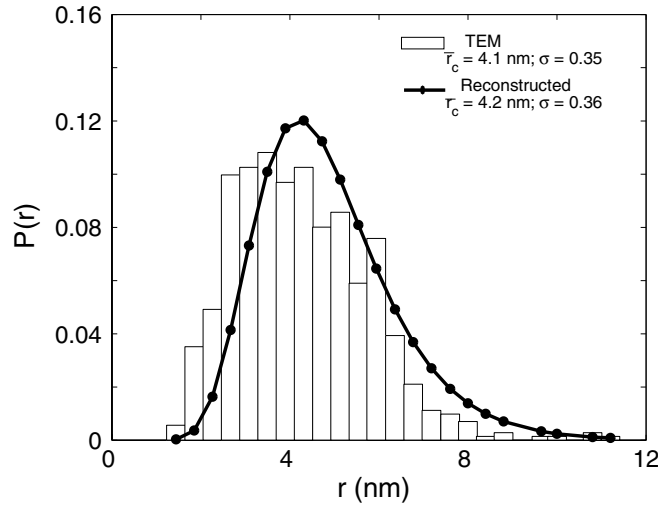


Figure 4. The reconstructed particle-size distribution along with the particle-size distribution obtained using TEM for comparisons (refer text in section 2.4 for details).

We test the procedure for extracting particle-size distribution from the susceptibility data on maghemite nanoparticle suspensions provided in [14]. From the Cole–Cole plots of these data, we evaluated the best-fit values of τ_c and β . These were found to be 2×10^{-8} s and 0.44, respectively. The average core radius \bar{r}_c , evaluated from τ_c using equation (2), was found to be 4.2 nm. The value of σ characterizing the spread of the log-normal distribution was then obtained using equation (12) and was found to be 0.36. The reconstructed particle-size distribution is shown in figure 4. The particle-size distribution obtained using TEM measurements has also been provided in the figure for comparisons. In general, we find that this procedure reproduces the original distributions rather well when the response function has one dominant peak, be it in the Néel or in the Brownian relaxation regime.

3. Clustering in MNP suspensions

The properties of the magnetic fluid are considerably affected by the aggregation of particles (in spite of surfactant coating) due to the presence of attractive and repulsive interactions. It is hence instructive to consider the different interaction energies in MNP suspensions and understand their interplay which leads to the formation of aggregates or clusters of different sizes.

3.1. Interactions in MNP suspensions

The primary interaction energies in these systems are enumerated below [1]:

1. *Dipolar interaction.* The dipolar interaction energy between two MNPs, each having a magnetic moment μ is given by

$$E_d(s) = -\frac{\mu_0}{4\pi} \left(\frac{3\mu \cdot (\mu \cdot \vec{s})\vec{s}}{s^5} - \frac{\mu^2}{s^3} \right), \quad (13)$$

where s is the center-to-center separation between the two nanoparticles and the permeability of free space $\mu_0 = 4\pi \times 10^{-7} \text{ H m}^{-1}$.

2. *van der Waal interaction.* This arises spontaneously between neutral particles because of the fluctuating electric dipolar forces and is attractive in nature. Hamaker calculated this interaction for identical spheres separated by a surface-to-surface distance l to be [19]

$$E_v = \frac{A}{6} \left\{ \frac{2}{l^2 + 4l} + \frac{2}{(l+2)^2} + \ln \left(\frac{l^2 + 4l}{l^2 + 4l + 4} \right) \right\}. \quad (14)$$

In the above equation, the Hamaker constant $A = 10^{-19} \text{ N m}$.

3. *Steric interaction.* The steric energy comes into play due to the presence of long chained surfactant molecules coating the particles. This mechanism prevents the particles from approaching very close to one another. This repulsive energy for spherical particles has been calculated by Papell and is given by [20]

$$E_s = \frac{E}{1.325} \left(2\delta - \frac{s}{2} \right)^{\frac{5}{2}} (r_c + \delta)^{\frac{1}{2}}. \quad (15)$$

In the above form, E is the Young's modulus which is usually of the order of 10^6 Pa for polymeric matrices and biological membranes.

Apart from the above interaction energies, the thermal energy responsible for the Brownian motion of the suspended particles also plays an important role in the aggregation dynamics. We expect the thermal degrees of freedom, in conjunction with steric repulsion, to not only hamper the aggregation process but also remove particles from the parent cluster leading to its fragmentation. At this juncture we define a parameter Ω as the ratio of energies leading to aggregation to those which lead to fragmentation as follows:

$$\Omega = \frac{E_d + E_v}{E_s + k_B T}. \quad (16)$$

It is expected that the distribution of cluster sizes and the mean-cluster size will be governed by the ratio Ω . In the following subsection, we present a model which incorporates the competing mechanisms of aggregation and fragmentation.

3.2. The aggregation–fragmentation model

The formulation introduced by Smoluchowski is especially useful to model a suspension of MNPs [21, 22]. To begin with, we assume that the suspension contains identical, single particles executing Brownian motion. The latter leads to aggregation of two particles if they come within an appropriate range of one another and the net interaction between them is attractive. The resulting cluster of size two also executes Brownian motion, but with a reduced diffusion rate till it encounters a particle or a cluster of particles. The process goes on and eventually a single large cluster comprising all the particles is formed. Such a cluster is usually referred to as an infinite aggregate. In most useful suspensions, however, there is a distribution of clusters of varying sizes. As discussed in the preceding subsection, the combined effects of thermal energy and inter-particle repulsion can introduce fragmentation in the cluster dynamics thereby preventing the formation of large aggregates. We thus include this additional mechanism in the rate equations which describe the evolution of clusters.

Let $P(k, t)$ denote the probability of having a cluster containing k particles at time t . The time evolution of $P(k, t)$ is governed by the following rate equations:

$$\frac{\partial P(k, t)}{\partial t} = \sum_{i+j=k} K_{ij} P(i, t)P(j, t) - P(k, t) \sum_{j=1}^{\infty} K_{kj} P(j, t) + \omega P(k+1, t) - \omega P(k, t), \quad k > 1, \quad (17)$$

$$\frac{\partial P(1, t)}{\partial t} = -P(1, t) \sum_{j=1}^{\infty} K_{1j} P(j, t) + \omega \sum_{j=2}^{\infty} P(j, t), \quad k = 1. \quad (18)$$

In equations (17) and (18), K_{ij} is the aggregation kernel which describes the coalescence of a cluster containing i particles with another containing j particles to yield a larger aggregate comprising $k = i + j$ particles. It is assumed to have a mass-dependent form defined by $K_{ij} = D(i^{-\mu} + j^{-\mu})$ to take into account the reduced mobility of large clusters. A value of $\mu = 0$ implies a mass-independent mobility, i.e. clusters of all sizes diffuse with the same ease. Non-zero values of μ results in a slower mobility of larger clusters and consequently a slower growth rate of clusters. In the limit of $\mu = \infty$, only monomers are mobile. The choice of μ is dictated by the experimental parameters as we shall see in a short while. The parameter ω , on the other hand, describes the loss or fragmentation of a particle from a parent cluster. The parameters D and ω define the relative strength of the aggregation and fragmentation processes.

The first and the third terms in equation (17) are referred to as the gain terms which result in the formation of clusters of size k . The former describes the aggregation of two clusters to yield a cluster containing k particles while the latter describes the generation of a cluster comprising k particles due to fragmentation of a particle from a cluster of size $k + 1$. The second and the fourth terms on the other hand, are referred to as the loss terms which describe processes leading to loss of clusters of size k . This could be due to aggregation of a cluster of size k with another or its fragmentation. The terms

of equation (18) can be interpreted similarly. It is easy to check that the following sum rule is satisfied:

$$\frac{\partial}{\partial t} \left(\sum_{k=1}^{\infty} P(k, t) \right) = 0 \quad \text{or} \quad \sum_{k=1}^{\infty} P(k, t) = 1, \quad (19)$$

as required by conservation conditions.

The condition $\partial P(k, t)/\partial t = 0$ describes the steady state which is of interest to us. In the absence of the fragmentation term, equation (17) reduces to the Smoluchowski equation describing coagulation phenomena [22]. There have been a few studies of this model, both analytical and numerical, to predict scaling forms associated with cluster growth and cluster-size distributions [23–29]. The growth of clusters with time is a power governed by the relation $\langle k(t) \rangle \sim t^z$. Choosing $\mu = 1$, the value of z was estimated to be $\simeq 0.5$. The steady state in this model was found to be an infinite (single) aggregate comprising all the N particles. Note that in the absence of fragmentation, the constant D can be absorbed by redefining t as Dt in equation (17), making the latter independent of the aggregation rate.

To mimic those physical situations which do not have an infinite aggregate as a steady state but rather have a distribution of clusters of varying sizes, it is essential to include fragmentation as a competing mechanism to aggregation. Of relevance in the context of this study is the model incorporating mass-independent aggregation and mass-dependent evaporation processes reported in [27]. The competition between aggregation and evaporation leads to several asymptotic outcomes of the steady-state solution of this model. For instance, if evaporation dominates over aggregation, the steady-state cluster-size distribution $P(k)$ versus k decays exponentially. On the other hand, for a critical evaporation rate, the distribution decays as $k^{-5/2}$.

3.3. Numerical results

We now solve the set of equations defined by equations (17) and (18) numerically to obtain the steady-state cluster-size distribution $P(k)$ versus k . It is useful to define the ratio R characterizing the relative strengths of the aggregation and fragmentation mechanisms:

$$R = \frac{D}{\omega}. \quad (20)$$

Identifying the physical origin of D in the attractive interactions between clusters and that of ω in the disordering agents (such as repulsive interactions and temperature), we can expect R to have the same qualitative effect as the ratio Ω defined in equation (16) on steady-state cluster-size distributions. We use this correspondence to bring contact between numerical results and experimental observations on cluster formation in MNP suspensions.

In figure 5(a), we look at the variation of the mean-cluster size $\langle k(R, t) \rangle$ as a function of t for different values of R on a double logarithmic scale. The parameter μ was chosen to be 2.0. After an initial growth period obeying a power law, the cluster size attains a steady-state value of $\langle k(R) \rangle$ due to

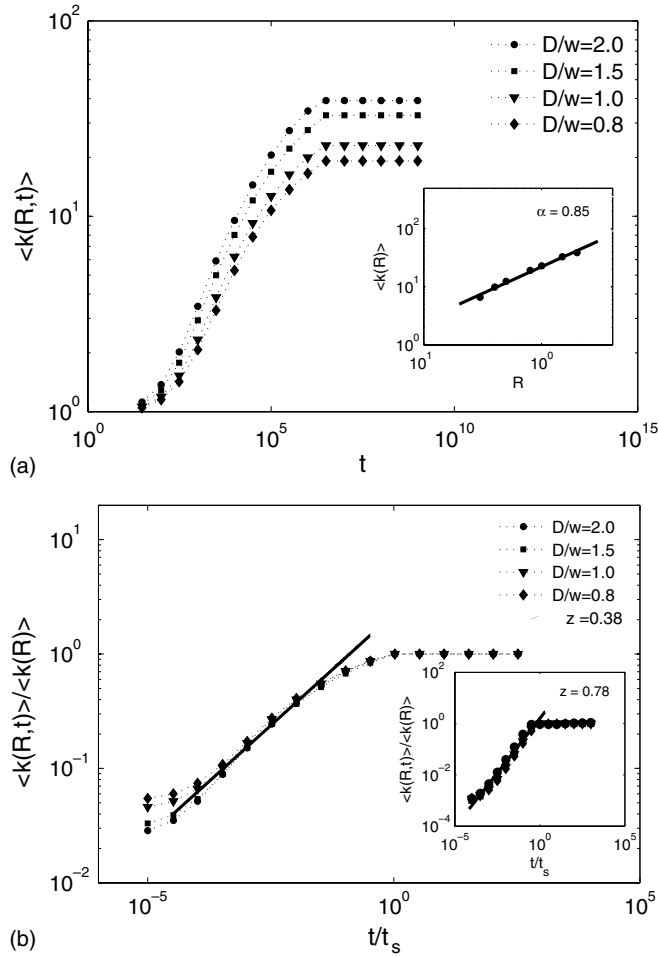


Figure 5. (a) Variation of the mean-cluster size $\langle k(R, t) \rangle$ as a function of time t for $\mu = 2$ and different values of the ratio R specified in the figure. The inset shows the steady-state value of the mean-cluster size $\langle k(R) \rangle$ as a function of R on a double logarithmic scale. The best-fit line to data has a slope 0.85 ± 0.02 , respectively. (b) Scaled data of (a) with the scaled axes as indicated in the figure. The initial growth of clusters obeys a power law characterized by the exponent $z = 0.38 \pm 0.02$. Similar data corresponding to $\mu = 1$ are also indicated in the inset. For these data, the growth exponent $z = 0.78 \pm 0.02$ as indicated.

the competing mechanisms of aggregation and fragmentation. As expected, $\langle k(R) \rangle$ increases with increasing values of R . In fact, we find that $\langle k(R) \rangle \sim R^\alpha$ with $\alpha = 0.85 \pm 0.02$ as can be seen in the inset. Further, in the diffusion-dominated regime ($R \gtrsim 0.5$) the data in figure 5(a) can be scaled by replotting $\langle k(R, t) \rangle / \langle k(R) \rangle$ versus t/t_s where t_s is the time taken to attain the steady state. The initial cluster growth is of the form $\langle k(t) \rangle \sim t^z$. We find that the growth exponent $z = 0.38 \pm 0.02$. The scaled data are shown in figure 5(b) on a double logarithmic scale. The best-fit line with a slope of 0.38 is also indicated. The value of the growth exponent also depends upon the value of μ . For $\mu = 1.0$, our simulations yield $z = 0.78 \pm 0.02$. The corresponding scaled data and the power law fit are also shown in the inset of figure 5(b). The faster growth of clusters is a consequence of increased mobility due to a lower value of μ .

Next in figure 6(a) we plot the steady-state distribution $P(k)$ versus k corresponding to $\mu = 2$ for the same set of

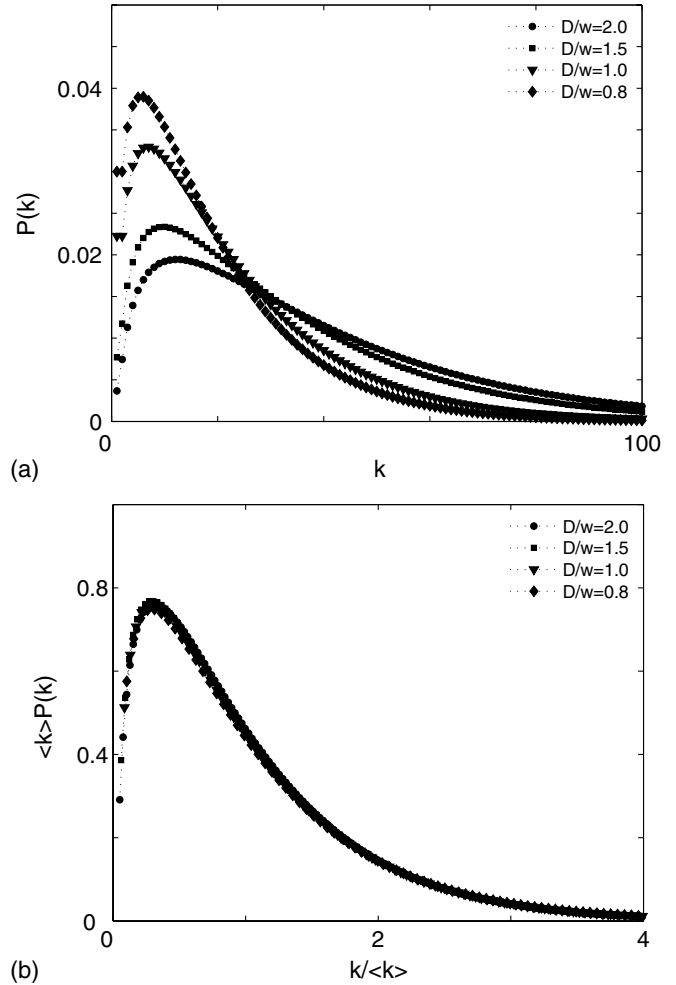


Figure 6. (a) Steady-state distribution $P(k)$ versus k for $\mu = 2$ for indicated values of ratio R . (b) Scaled data of (a) with the scaled axis as indicated in the figure.

R values considered above. We find that the tails of the distributions fit well to a power law in k . In figure 6(b), we plot $\langle k(R) \rangle P(k)$ versus $k/\langle k(R) \rangle$ where $\langle k(R) \rangle$ is the steady-state average cluster size for the corresponding value of R . These plots indicate that the distribution functions $P(k)$ corresponding to different values of R obey scaling in the diffusion-dominated regime. The scaling relation can be summarized in the following equation:

$$P(k) = \frac{1}{\langle k(R) \rangle} f\left(\frac{k}{\langle k(R) \rangle}\right), \quad \langle k(R) \rangle \sim R^\alpha. \quad (21)$$

3.4. Comparisons with experimental data

We now compare our simulation results with the experimental data on average cluster sizes in a variety of MNP suspensions. Eberbeck *et al* studied the aggregation of various MNPs in a variety of media such as water, phosphate buffered saline, calf serum, bovine serum and human serum [30, 31]. The experimental measurements were performed at room temperature. In all cases, formation of dimers and trimers were reported by the authors. To make comparisons with the simulation results of our model, we first calculate the ratio Ω

Table 2. Calculated value of the ratio Ω and the corresponding estimated value of the cluster size for a variety of MNP used in experiments by Eberbeck *et al* [30, 31]. The experimental parameters associated with each sample are also specified.

MNP sample	Core	Shell	Ω	$\langle k \rangle$
DDN128	Fe ₃ O ₄	carboxydextran	0.5364	2.3
FluidMagD5	Fe ₃ O ₄	starch	0.36	2.0
MagBSA	Fe ₃ O ₄	BSA	0.676	2.5
Resovist	Fe ₃ O ₄	Carboxydextran	0.51	2.4

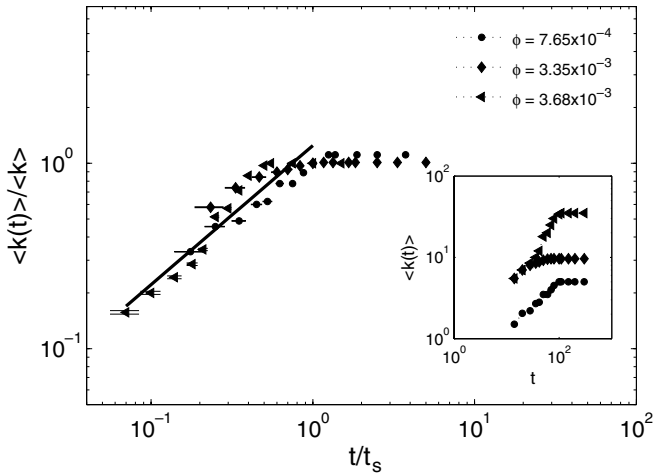


Figure 7. Data from [8] on average chain length as a function of time for different volume fractions replotted on scaled axes as shown in the figure. The solid line corresponds to a slope of 0.78 obtained from a numerical solution of the aggregation–fragmentation model with $\mu = 1$ (refer the inset of figure 5(b) and corresponding text).

defined in equation (16) for each of the samples. These along with the sample specifications are tabulated in table 2. As can be seen in column 4, Ω is in the range 0.35–0.70. Referring to the plot of $\langle k(R) \rangle$ versus R for $\mu = 2$ in the inset of figure 5(a), a value of R in the above range yields dimers and trimers in the steady state.

A set of experimental measurements which we find especially relevant in the context of the aggregation–fragmentation model are reported in [8]. In this paper, the authors have studied aggregation dynamics in very dilute emulsions of ferrofluid droplets in water. The ferrofluid droplets were small Fe₃O₄ grains in kerosene coated with a surfactant to prevent agglomeration. The data on average chain lengths as a function of time for different volume fractions and applied fields were obtained using dynamic light scattering experiments. We reproduce a scaled form of these data in figure 7. On the x -axis, we plot t/t_s , where t_s is the time taken to reach the steady-state value of the average cluster. The y -axis has been scaled by the steady-state value of the average chain length. The unscaled data are also provided in the inset for reference. As can be observed in figure 7, the scaled form (as well as the unscaled form) of the experimental data bears a qualitative resemblance to figure 5(b) which results from the numerical solution of the aggregation–fragmentation model defined by equations (17) and (18). The slow initial growth, the power law form at intermediate times and saturation to a

steady-state value as time progresses are borne by both sets of data.

On the quantitative side, we find that the experimental data are well represented by a growth exponent $z = 0.78 \pm 0.02$ obtained with $\mu = 1$ in our simulations. The corresponding line is depicted in figure 7. It is pertinent to recall here that the dipolar interaction becomes dominant in the presence of the applied magnetic field thereby increasing the diffusivity of the clusters. In the aggregation–fragmentation model, the latter can be achieved by an increase in the value D as well as a decrease in the value of μ . Consequently, we find that our data on $\langle k(R, t) \rangle$ versus t for a value of $\mu = 1$ rather than $\mu = 2$ results in accurate comparisons with the experimental data. We note here that theoretical studies on systems of this kind were so far based on Smoluchowski kinetic equations for irreversible aggregation [23, 24]. However, the observed growth exponent does not conform with the predicted value of $z = 0.5$ (also obtained with $\mu = 1$) of this model.

A similar set of experimental results were obtained in [9] where the power law prediction for cluster growth was checked by performing a large number of experiments on aqueous solutions of super paramagnetic polystyrene beads having a uniform distribution of Fe₃O₄ particles. The data were obtained for five values of the volume fraction in the presence of low field strengths and higher field strength using optical microscopy. The exponent z describing the cluster growth in these studies was found to be much larger than the predicted value of 0.5 especially for small volume fractions and low field strengths. These observations further reiterate the appropriateness of introducing fragmentation along with aggregation especially in the above limits where the thermal energy plays a significant role in the dynamics.

4. Summary

We conclude this paper with a summary of results presented here. Our main interest was to understand the factors governing the dynamical response of suspensions of single-domain MNPs. Such an understanding introduces the possibility of synthesizing particles with application tailored response times. The effect of sample parameters on the Néel and Brownian relaxation times which characterize the response was studied. Amongst all the parameters of relevance, the anisotropy of the constituting material and the particle size alter the relaxation time most significantly. In fact, the dominant relaxation time is also decided primarily by the particle size. We also studied how these parameters affect the ac susceptibility $\chi(\omega)$ which is the most commonly studied response function in the laboratory. This understanding proves to be useful in estimating relaxation times as well as sample parameters from the measurement of $\chi(\omega)$ in the laboratory.

We have then studied the effect of polydispersity, an inherent feature of all samples on the response characteristics. These exhibit significant changes due to the strong dependence of relaxation times on particle sizes. The primary effect is the broadening of response functions and in some cases the latter exhibits a two peaked structure. We have also worked

out a procedure to obtain the particle-size distribution from $\chi(\omega)$ using Cole–Cole plots and the analysis of Cole and Davidson. This provides an alternative procedure to TEM analysis which is usually employed to obtain particle-size distributions.

The above studies assumed a single-particle model applicable to dilute suspensions. However, in many cases the inter-particle interactions cannot be ignored. Clustering of particles is inevitable in such suspensions. While the formation of clusters is undesirable in some applications, it is beneficial in many others. Hence, we have tried to understand the mechanisms responsible for clustering and the experimental parameters which govern the properties of cluster-size distribution and the average cluster size. This knowledge is useful for the synthesis of application tailored suspensions.

A model incorporating the phenomena of aggregation and fragmentation was used to understand aspects of clustering. The steady-state cluster-size distributions of the model were obtained by numerically solving the rate equations describing the evolution of clusters. We have obtained scaling forms for the cluster-size distributions and the average cluster size. Our results agree well with experiments where clustering or chain formation has been observed.

An interesting extension of this work is to small ferromagnetic particles with an antiferromagnetic coating which have recently generated considerable research interest [32–34]. The resulting ferromagnetic–antiferromagnetic interfaces, under suitable experimental conditions, yield an anisotropy referred to as exchange bias. The latter results in locking of the magnetic moment of the superparamagnetic particle. As a result, we can expect the relaxation behaviour of these particles to be quite different from that of superparamagnetic particles considered in this paper. At present, we are attempting to develop a theoretical framework to understand the response behaviour of a suspension MNPs with exchange bias. We believe that it will be possible to formulate the necessary arguments.

Acknowledgments

VS and VB would like to acknowledge the support of CSIR Grant No 03(1077)/06/EMR-II. VB would also like to acknowledge the hospitality of ICTP, Italy, where part of the work was completed.

References

- [1] Rosensweig R E 1997 *Ferrohydrodynamics* (New York: Dover)
- [2] Odenbach S 2002 *Magnetoviscous Effects in Ferrofluids* (Berlin: Springer)
- [3] Coffey W T, Kalmykov Yu P and Waldron J T 1996 *The Langevin Equation* (Singapore: World Scientific)
- [4] Pankhurst Q A, Connolly J, Jones S K and Dobson J 2003 *J. Phys. D: Appl. Phys.* **36** R167
- [5] Astalan A P, Ahrentrop F, Johansson C, Larsson K and Krozer A 2004 *Biosensors Bioelectron.* **19** 945
- [6] Chung S, Hoffmann A and Bader S A 2004 *Appl. Phys. Lett.* **85** 2971
- [7] Shliomis M I and Raikher Y 1980 *IEEE Trans. Magn.* **16** 237
- [8] Promislow J H E, Gast A P and Fermigier M 1995 *J. Chem. Phys.* **102** 5492
- [9] Hagenbuchle M and Liu J 1997 *Appl. Opt.* **36** 7664
- [10] Kellner R R and Kohler W 2005 *J. Appl. Phys.* **97** 034910
- [11] Hasmonay E and Depeyrot J 2000 *J. Appl. Phys.* **88** 6628
- [12] Dattagupta S 1987 *Relaxation Phenomena in Condensed Matter Physics* (Orlando: Academic)
- [13] Brown W F 1963 *J. Appl. Phys.* **34** 1319
- [14] Fannin P C and Charles S W 1989 *J. Phys. D: Appl. Phys.* **22** 187
- [15] Fannin P C, Relihan T and Charles S W 1997 *Phys. Rev B* **55** 14423
- [16] Cole K S and Cole R H 1941 *J. Chem. Phys.* **9** 341
- [17] Cole K S and Cole R H 1942 *J. Chem. Phys.* **10** 98
- [18] Davidson D W and Cole R H 1951 *J. Chem. Phys.* **19** 1484
- [19] Hamaker H C 1937 *Physica* **4** 1058
- [20] Pappel S S 1964 US Patent 3215572
- [21] Smoluchowski M V 1916 *Z. Phys.* **17** 585
- [22] Chandrasekhar S 1943 *Stochastic problems in physics and astronomy Rev. Mod. Phys.* **15** 1
- [23] Miyazima S, Meakin P and Family F 1987 *Phys. Rev. A* **36** 1421
- [24] Kandel D 1997 *Phys. Rev. Lett.* **79** 4238
- [25] Morimoto H and Maekawa T 2000 *J. Phys. A: Math. Gen.* **33** 247
- [26] Ernst M H and Dongen P G J 1987 *Phys. Rev. A* **36** 435
- [27] Krapivsky P L and Redner S 1996 *Phys. Rev. E* **54** 3553
- [28] Chavez F, Moreau M and Vicente L 1997 *J. Phys. A.: Math. Gen.* **30** 6615
- [29] Kalachev L, Morimoto H and Maekawa T 2001 *Int. J. Mod. Phys. B* **15** 774
- [30] Eberbeck D, Wiekhorst F, Steinhoff U and Trahms L 2006 *J. Phys.: Condens. Matter* **18** S2829
- [31] Eberbeck D, Bergemann C, Hartwig S, Steinhoff U and Trahms L 2005 *J. Magn. Magn. Mater.* **289** 435
- [32] Noguez J and Schuller I K 1999 *J. Magn. Magn. Mater.* **192** 203
- [33] Eftaxias E and Trohidon K N 2005 *Phys. Rev. B* **71** 134406
- [34] Iglesias O, Battle X and Labarta A 2005 *Phys. Rev. B* **72** 212401